Optics and Lasers in Engineering 57 (2014) 28–39

Contents lists available at ScienceDirect

Optics and Lasers in Engineering

journal homepage: www.elsevier.com/locate/optlaseng

Quaternion higher-order spectra and their invariants for color image recognition

Xiaoning Jia [a,*], Hang Yang [b], Siliang Ma [a], Dongzhe Song [a]

[a] College of Mathematics, Jilin University, Changchun, Jilin Province 130012, China
[b] Changchun Institute of Optics, Fine Mechanics and Physics, Chinese Academy of Science, Changchun 130033, China

ARTICLE INFO

Article history:
Received 13 February 2013
Received in revised form
9 December 2013
Accepted 9 January 2014
Available online 29 January 2014

Keywords:
Color image recognition
Quaternion
Bispectrum
Higher-order spectra invariant
Quaternion principal component analysis

ABSTRACT

This paper describes an invariants generation method for color images, which could be a useful tool in color object recognition tasks. First, by using the algebra of quaternions, we introduce the definition of quaternion higher-order spectra (QHOS) in the spatial domain and derive its equivalent form in the frequency domain. Then, QHOS invariants with respect to rotation, translation, and scaling transformations for color images are constructed using the central slice theorem and quaternion bispectral analysis. The feature data are further reduced to a smaller set using quaternion principal component analysis. The proposed method can deal with color images in a holistic manner, and the constructed QHOS invariants are highly immune to background noise. Experimental results show that the extracted QHOS invariants form compact and isolated clusters, and that a simple minimum distance classifier can yield high recognition accuracy.

© 2014 Elsevier Ltd. All rights reserved.

1. Introduction

A major issue in visual pattern recognition is to extract features that are invariant to geometric transformations, such as rotation, translation, and scaling (RTS), and have high noise immunity. The problem of invariant feature extraction for robust pattern recognition is complex and difficult [1]. Various techniques have been proposed in the literature to deal with it. For example, the frequency domain methods based on the Fourier descriptors [2–5] can maintain local information well, but some useful information contained in the phase component of the Fourier transform is ignored. The moment invariants methods [6–9] are also usually used owing to their image description capability and invariance property. However, they are vulnerable to background noise.

Higher-order spectra (HOS) [10–12] have been introduced as spectral representation of stochastic and deterministic signals. The use of HOS for feature extraction is motivated by the following: (1) HOS retain both amplitude and phase information about the Fourier coefficients of a signal and the Fourier phase contains important shape information; (2) HOS are translation invariant and it is also easier to define features from HOS that satisfy other desirable invariance properties; (3) HOS are zero for Gaussian noise and, thus, provide high noise immunity to features; and (4) multidimensional signals can be decomposed into 1-D projections, then HOS features derived from the projections can be used to derive invariant features for the multidimensional signals. As a result, HOS, in particular the third-order spectra (bispectra), have been extensively used for signal detection and object identification [13–16]. However, HOS are mainly used to deal with gray-level images in those papers.

With the development of image acquisition devices, almost all images acquired are chromatic nowadays. In general, there are two approaches to processing color images. The first one transforms the color image into gray-scale one, which may lose some significant color information. The second one decomposes the color image into three channels, and then processes each channel separately, which may ignore the vectorial nature of color images. These problems have not been solved until quaternions, formally introduced by Hamilton in 1843 [17], are introduced to represent color images by Ell and Sangwine [18–20]. The main advantage of the use of quaternion-type representation is that an RGB image can be treated as a vector field by encoding its three channel components on the three imaginary parts of a pure quaternion and, thus, can be processed holistically. Recently, some traditional moment functions are generalized to quaternion algebra, such as quaternion Fourier–Mellin moments (QFMMs) [21] and quaternion Zernike moments (QZMs) [22], and then a set of quaternion moment invariants with respect to RTS transformations are constructed for color images. Although good performance is obtained, when the number of invariant features increases, the invariants

* Correspondence to: College of Mathematics, Jilin University, Qianjin Street No. 2699, Chaoyang District, Changchun, Jilin Province 130012, China.
Tel.: +8613756318021.
E-mail address: jiaxn11@mails.jlu.edu.cn (X. Jia).

0143-8166/$ - see front matter © 2014 Elsevier Ltd. All rights reserved.
http://dx.doi.org/10.1016/j.optlaseng.2014.01.008

are vulnerable to background noise, especially for the higher-order moment invariants.

Ell [18] introduced quaternion Fourier transforms (QFTs). Since then, QFTs have been successfully applied in color image registration [23], watermarking [24], motion estimation [25] and texture analysis [26]. Enlightened by the definition of QFTs, we generalize the traditional HOS from real numbers to quaternion algebra. Quaternion higher-order spectra (QHOS) are introduced and a set of QHOS invariants with respect to RTS transformations are constructed for color images. The derived QHOS invariants are highly immune to symmetrically distributed background noise, such as white Gaussian and uniform noise. The remaining parts of this paper are organized as follows. Section 2 introduces the definition of QHOS and derives its equivalent form in the frequency domain. Section 3 proposes the RTS invariants generation algorithm using the central slice theorem, quaternion bispectra, and quaternion principal component analysis. Experimental results are presented and discussed in Section 4. Section 5 provides the concluding remarks.

2. Quaternion higher-order spectra

2.1. QHOS in the spatial domain

Readers unfamiliar with quaternions and QFTs may wish at this point to read Appendix A, where a review of their mathematical concepts pertinent to this paper is given. For a more detailed treatment, the book by Ward [27] is recommended.

Let $f(t)$ be a real-valued, zero-mean 1-D signal, the traditional third-order spectrum, called bispectrum, of $f(t)$ is defined as

$$B(\omega,\nu)=\int_{-\infty}^{\infty}\int_{-\infty}^{\infty}M(x,y)e^{-\mathrm{i}(\omega x+\nu y)}dxdy, \tag{1}$$

where $M(x,y)$ is the third-order moment of $f(t)$ given by

$$M(x,y)=\begin{cases}\int_{-\infty}^{\infty}f(t)f(t+x)f(t+y)dt, & \text{for deterministic process;}\\ E[f(t)f(t+x)f(t+y)], & \text{for stationary random process.}\end{cases} \tag{2}$$

When the signal $f(t)$ is corrupted by additive, independent and identically distributed (i.i.d.), symmetrical noise, its third-order moment $M(x,y)$ remains unchanged [28]. Combined with the 2-D QFTs, the traditional bispectra defined above can be generalized to quaternion algebra.

Definition 1. Let $f(t)$ be a quaternion-valued, zero-mean 1-D signal, the right-side quaternion bispectrum of $f(t)$ is given by

$$B^{R}(\omega,\nu)=\int_{-\infty}^{\infty}\int_{-\infty}^{\infty}M(x,y)e^{-\mu(\omega x+\nu y)}dxdy, \tag{3}$$

where μ is a unit pure quaternion, and $M(x,y)$ is the third-order moment of $f(t)$ defined in the same way as Eq. (2). It is straightforward to demonstrate that the third-order moment $M(x,y)$ of a quaternion-valued signal $f(t)$ also remains unchanged when it is corrupted by additive, i.i.d., symmetrical noise.

Based on the discrete 2-D QFTs, we have the following discrete form of the right-side quaternion bispectrum for a deterministic signal $f(t)$:

$$B^{R}(\omega,\nu)=\sum_{x=-N+1}^{N-1}\sum_{y=-N+1}^{N-1}\sum_{t=0}^{N-1}f(t)f(t+x)f(t+y)e^{-\mu 2\pi((\omega x+\nu y)/(2N-1))}, \tag{4}$$

where N is the sequence length of $f(t)$.

Similar as the definition of QFTs, we can define the left-side and two-side quaternion bispectra as

$$B^{L}(\omega,\nu)=\int_{-\infty}^{\infty}\int_{-\infty}^{\infty}e^{-\mu(\omega x+\nu y)}M(x,y)dxdy, \tag{5}$$

$$B^{RL}(\omega,\nu)=\int_{-\infty}^{\infty}\int_{-\infty}^{\infty}e^{-\mu_1\omega x}M(x,y)e^{-\mu_2\nu y}dxdy. \tag{6}$$

where μ_1 and μ_2 are two unit pure quaternions that are orthogonal to each other. The corresponding discrete forms are

$$B^{L}(\omega,\nu)=\sum_{x=-N+1}^{N-1}\sum_{y=-N+1}^{N-1}\sum_{t=0}^{N-1}e^{-\mu 2\pi((\omega x+\nu y)/(2N-1))}f(t)f(t+x)f(t+y), \tag{7}$$

$$B^{RL}(\omega,\nu)=\sum_{x=-N+1}^{N-1}\sum_{y=-N+1}^{N-1}\sum_{t=0}^{N-1}e^{-\mu_1 2\pi(\omega x/(2N-1))}f(t)f(t+x)f(t+y)e^{-\mu_2 2\pi(\nu y/(2N-1))}. \tag{8}$$

In this paper, the quaternion bispectra refer to the right-side quaternion bispectra and denoted as $B(\omega,\nu)$.

2.2. QHOS in the frequency domain

The traditional bispectra, defined by Eq. (1), can be rewritten directly in the frequency domain as

$$B(\omega,\nu)=F(\omega)F(\nu)\overline{F(\omega+\nu)}, \tag{9}$$

where $F(\cdot)$ is the Fourier transform of $f(t)$. As the multiplication of quaternions is not commutative, Eq. (9) cannot be generalized to quaternion algebra directly. However, by doing a suitable decomposition to the quaternion-valued function $f(t)$, we can still redefine the quaternion bispectra directly in the frequency domain.

Suppose that the unit pure quaternion $\mu=\mu_i i+\mu_j j+\mu_k k$, then, we can rewrite a quaternion-valued signal $f(t)=f_r(t)+f_i(t)i+f_j(t)j+f_k(t)k$ as

$$f(t)=f_r(t)+f_0(t)\mu+f_1(t)\mu_1+f_2(t)\mu_2\triangleq f_a(t)+f_b(t)\mu_1, \tag{10}$$

where $\mu_1=\mu_{1i}i+\mu_{1j}j+\mu_{1k}k$, $\mu_2=\mu\mu_1=\mu_{2i}i+\mu_{2j}j+\mu_{2k}k$ are two unit pure quaternions, both of which are orthogonal to μ, and $f_a(t)=f_r(t)+f_0(t)\mu$, $f_b(t)=f_1(t)+f_2(t)\mu$. The relation between $f_0(t)$, $f_1(t)$, $f_2(t)$ and $f_i(t)$, $f_j(t)$, $f_k(t)$ is

$$\begin{pmatrix}f_0(t)\\ f_1(t)\\ f_2(t)\end{pmatrix}=\begin{pmatrix}\mu_i & \mu_{1i} & \mu_{2i}\\ \mu_j & \mu_{1j} & \mu_{2j}\\ \mu_k & \mu_{1k} & \mu_{2k}\end{pmatrix}^{-1}\begin{pmatrix}f_i(t)\\ f_j(t)\\ f_k(t)\end{pmatrix}. \tag{11}$$

Theorem 1. *The quaternion bispectra $B(\omega,\nu)$ in Eq. (3) can be redefined as*

$$\begin{aligned}B(\omega,\nu)=&F_a(-\omega-\nu)F_a(\omega)F_a(\nu)+F_b(\omega+\nu)\mu_1F_a(\omega)F_a(\nu)\\&+F_a(\omega+\nu)F_b(-\omega)\mu_1F_a(\nu)+F_b(-\omega-\nu)\mu_1F_b(-\omega)\mu_1F_a(\nu)\\&+F_a(\omega+\nu)F_a(-\omega)F_b(-\nu)\mu_1\\&+F_b(-\omega-\nu)\mu_1F_a(-\omega)F_b(-\nu)\mu_1\\&+F_a(-\omega-\nu)F_b(\omega)\mu_1F_b(-\nu)\mu_1\\&+F_b(\omega+\nu)\mu_1F_b(\omega)\mu_1F_b(-\nu)\mu_1,\end{aligned} \tag{12}$$

where $F_a(\cdot)$ and $F_b(\cdot)$ are the 1-D QFTs of $f_a(t)$ and $f_b(t)$ in Eq. (10), respectively.

Proof. To prove Eq. (12), we need to use the following properties of μ and μ_1:

$$\begin{cases}e^{\mu t}(a+b\mu)=(a+b\mu)e^{\mu t},\\ \mu\mu_1=-\mu_1\mu,\\ \mu_1e^{\mu t}=e^{-\mu t}\mu_1,\end{cases} \tag{13}$$

where a and b are real numbers. Eq. (13) can be demonstrated by simple calculations.

By substituting $f(t)=f_a(t)+f_b(t)\mu_1$ and using Eq. (13), Eq. (3) can be rewritten as

$$\begin{aligned}B(\omega,\nu)&=\int_{-\infty}^{\infty}\int_{-\infty}^{\infty}\int_{-\infty}^{\infty}[f_a(t)+f_b(t)\mu_1][f_a(t+x)+f_b(t+x)\mu_1][f_a(t+y)\\&\quad+f_b(t+y)\mu_1]e^{-\mu(\omega x+\nu y)}dtdxdy\\&=\int_{-\infty}^{\infty}\int_{-\infty}^{\infty}[f_a(t)+f_b(t)\mu_1][f_a(t+x)+f_b(t+x)\mu_1]\\&\quad\int_{-\infty}^{\infty}[f_a(t+y)e^{-\mu\nu(t+y)}+f_b(t+y)e^{\mu\nu(t+y)}\mu_1]dye^{\mu\nu t}e^{-\mu\omega x}dtdx\\&=\int_{-\infty}^{\infty}\int_{-\infty}^{\infty}[f_a(t)+f_b(t)\mu_1][f_a(t+x)+f_b(t+x)\mu_1][F_a(\nu)\\&\quad+F_b(-\nu)\mu_1]e^{\mu\nu t}e^{-\mu\omega x}dtdx\\&=\int_{-\infty}^{\infty}[f_a(t)+f_b(t)\mu_1]\{[F_a(\omega)+F_b(-\omega)\mu_1]F_a(\nu)+[F_a(-\omega)\\&\quad+F_b(\omega)\mu_1]F_b(-\nu)\mu_1\}e^{\mu(\omega+\nu)t}dt\\&=F_a(-\omega-\nu)F_a(\omega)F_a(\nu)+F_b(\omega+\nu)\mu_1F_a(\omega)F_a(\nu)\\&\quad+F_a(\omega+\nu)F_b(-\omega)\mu_1F_a(\nu)+F_b(-\omega-\nu)\mu_1F_b(-\omega)\mu_1F_a(\nu)\\&\quad+F_a(\omega+\nu)F_a(-\omega)F_b(-\nu)\mu_1+F_b(-\omega-\nu)\mu_1F_a(-\omega)F_b(-\nu)\mu_1\\&\quad+F_a(-\omega-\nu)F_b(\omega)\mu_1F_b(-\nu)\mu_1+F_b(\omega+\nu)\mu_1F_b(\omega)\mu_1F_b(-\nu)\mu_1.\end{aligned}\tag{14}$$

3. QHOS invariants for color images

In this section, we describe an invariants generation method for 2-D color images, which is based on the Radon transform or the central slice theorem, quaternion bispectra, and quaternion principal component analysis. The derived invariants are proved to be independent of image rotation, translation, and scaling.

3.1. The Radon transform and the central slice theorem

Let $f(x,y)=f_R(x,y)i+f_G(x,y)j+f_B(x,y)k$ represents an RGB image, the Radon transform, denoted by $R(s,\theta)$, is the 1-D projection of $f(x,y)$ at the angle θ, which is also a pure-quaternion-valued function, given by

$$R(s,\theta)=\int_{-\infty}^{\infty}f(s\ \cos\ \theta-t\ \sin\ \theta, s\ \sin\ \theta+t\ \cos\ \theta)dt,\quad -\infty<s<\infty, 0\le\theta<\pi.\tag{15}$$

The Radon transform has useful properties about image rotation, translation, and scaling as follows:

$$\text{translation}:\ f(x-x_0,y-y_0)\Leftrightarrow R(s-x_0\ \cos\ \theta-y_0\ \sin\ \theta,\theta);\tag{16}$$

$$\text{scaling}:\ f(ax,ay)\Leftrightarrow\frac{1}{|a|}R(as,\theta),\ a\text{ is real and }a\neq 0;\tag{17}$$

$$\text{rotation}:\ f_p(r,\rho+\alpha)\Leftrightarrow R(s,\theta+\alpha),\tag{18}$$

where $f_p(r,\rho)$ is the polar coordinate representation of $f(x,y)$.

The existence of the central slice theorem (also called the central projection theorem) enables the implementation of the Radon transform efficient by using the Fast Fourier Transform (FFT) algorithm. It can be seen from the definition of QFTs that the central slice theorem still holds in quaternion algebra.

Proposition 1. (The central slice theorem) Let $f(x,y)$ be a pure-quaternion-valued RGB image, the 1-D QFT of its Radon transform $R(s,\theta)$ with s being a variable and θ being a parameter, denoted by $F_s(\omega,\theta)$, is equal to the central slice at the angle θ of its 2-D QFT, denoted by $F_{x,y}(\omega\ \cos\ \theta,\omega\ \sin\ \theta)$, that is

$$F_s(\omega,\theta)=F_{x,y}(\omega\ \cos\ \theta,\omega\ \sin\ \theta).\tag{19}$$

3.2. The QHOS invariants generation scheme

According to the definition given by Eqs. (3) and (12), the quaternion bispectrum of a 1-D sequence is a 2-D function, and the bispectrum of a 2-D image is a 4-D function. To avoid the computational complexity, the original 2-D RGB image $f(x,y)$ is first reduced to a set of 1-D functions, which can be implemented directly in the spatial domain via the Radon transform or indirectly in the frequency domain via the central slice theorem. In the spatial domain, the quaternion bispectrum of the Radon transform $R(s,\theta)$ of $f(x,y)$, denoted by $B_\theta(\omega,\nu)$, can be computed using

$$B_\theta(\omega,\nu)=\int_{-\infty}^{\infty}\int_{-\infty}^{\infty}\int_{-\infty}^{\infty}R(s,\theta)R(s+x,\theta)R(s+y,\theta)e^{-\mu(\omega x+\nu y)}dsdxdy.\tag{20}$$

If rewriting $f(x,y)=f_a(x,y)+f_b(x,y)\mu_1$ by Eqs. (10) and (11), as mentioned in Section 2.2, according to Theorem 1 and the central slice theorem, the quaternion bispectrum $B_\theta(\omega,\nu)$ in Eq. (20) can be computed directly in the frequency domain using

$$\begin{aligned}B_\theta(\omega,\nu)&=F_{a,\theta}(-\omega-\nu)F_{a,\theta}(\omega)F_{a,\theta}(\nu)+F_{b,\theta}(\omega+\nu)\mu_1F_{a,\theta}(\omega)F_{a,\theta}(\nu)\\&\quad+F_{a,\theta}(\omega+\nu)F_{b,\theta}(-\omega)\mu_1F_{a,\theta}(\nu)\\&\quad+F_{b,\theta}(-\omega-\nu)\mu_1F_{b,\theta}(-\omega)\mu_1F_{a,\theta}(\nu)\\&\quad+F_{a,\theta}(\omega+\nu)F_{a,\theta}(-\omega)F_{b,\theta}(-\nu)\mu_1\\&\quad+F_{b,\theta}(-\omega-\nu)\mu_1F_{a,\theta}(-\omega)F_{b,\theta}(-\nu)\mu_1\\&\quad+F_{a,\theta}(-\omega-\nu)F_{b,\theta}(\omega)\mu_1F_{b,\theta}(-\nu)\mu_1\\&\quad+F_{b,\theta}(\omega+\nu)\mu_1F_{b,\theta}(\omega)\mu_1F_{b,\theta}(-\nu)\mu_1,\end{aligned}\tag{21}$$

where $F_{a,\theta}(\cdot)$ and $F_{b,\theta}(\cdot)$ are the central slices at the angle θ of the 2-D QFTs of $f_a(x,y)$ and $f_b(x,y)$, respectively. If we rewrite $R(s,\theta)=R_a(s,\theta)+R_b(s,\theta)\mu_1$,$F_{a,\theta}(\cdot)$ and $F_{b,\theta}(\cdot)$ are actually the 1-D QFTs of $R_a(s,\theta)$ and $R_b(s,\theta)$ with s being a variable and θ being a parameter. In this paper, Eq. (21) is applied for the implementation of the proposed QHOS invariants generation method.

Theorem 2. *Let*

$$\Phi(\theta)=\frac{\int_{-\infty}^{\infty}\int_{-\infty}^{\infty}B_\theta(\omega,\nu)d\omega d\nu}{\|\int_{-\infty}^{\infty}\int_{-\infty}^{\infty}B_\theta(\omega,\nu)d\omega d\nu\|},\tag{22}$$

then, $\Phi(\theta)$ is invariant to image translation and scaling.

Proof. Let $f(x-x_0,y-y_0)$ be a shifted version of $f(x,y)$, according to Eq. (16), the resultant Radon transform $R'(s,\theta)$ of $f(x-x_0,y-y_0)$ becomes $R(s-s_0,\theta)$, where $s_0=x_0\ \cos\ \theta+y_0\ \sin\ \theta$. Then, the quaternion bispectrum$B'_\theta(\omega,\nu)$ of $R'(s,\theta)$ is given by

$$\begin{aligned}B'_\theta(\omega,\nu)&=\int_{-\infty}^{\infty}\int_{-\infty}^{\infty}\int_{-\infty}^{\infty}R'(s,\theta)R'(s+x,\theta)R'\\&\quad(s+y,\theta)e^{-\mu(\omega x+\nu y)}dsdxdy\\&=\int_{-\infty}^{\infty}\int_{-\infty}^{\infty}\int_{-\infty}^{\infty}R(s-s_0,\theta)R(s-s_0+x,\theta)R\\&\quad(s-s_0+y,\theta)e^{-\mu(\omega x+\nu y)}dsdxdy\\&=\int_{-\infty}^{\infty}\int_{-\infty}^{\infty}\int_{-\infty}^{\infty}R(s,\theta)R(s+x,\theta)R(s+y,\theta)e^{-\mu(\omega x+\nu y)}dsdxdy\\&=B(\omega,\nu).\end{aligned}\tag{23}$$

Therefore, $\Phi(\theta)$ defined by Eq. (22) is translation invariant.

Let $f(ax,ay)$ be a scaled version of $f(x,y)$, where $a\neq 0$, according to Eq. (17), the resultant Radon transform $R'(s,\theta)$ of $f(ax,ay)$ is $R(as,\theta)/|a|$. Then, the corresponding quaternion bispectrum

$B'_\theta(\omega,\nu)$ becomes

$$\begin{aligned}B'_\theta(\omega,\nu) &= \int_{-\infty}^{\infty}\int_{-\infty}^{\infty}\int_{-\infty}^{\infty} R'(s,\theta)R'(s+x,\theta)R'\\ &\quad (s+y,\theta)e^{-\mu(\omega x+\nu y)}dsdxdy\\ &= \frac{1}{|a|^3}\int_{-\infty}^{\infty}\int_{-\infty}^{\infty}\int_{-\infty}^{\infty} R(as,\theta)R(as+ax,\theta)R\\ &\quad (as+ay,\theta)e^{-\mu(\omega x+\nu y)}dsdxdy\\ &= \frac{1}{a^6}\int_{-\infty}^{\infty}\int_{-\infty}^{\infty}\int_{-\infty}^{\infty} R(s,\theta)R(s+x,\theta)R\\ &\quad (s+y,\theta)e^{-\mu(((\omega/a)x)+((\nu/a)y))}dsdxdy\\ &= \frac{1}{a^6}B\left(\frac{\omega}{a},\frac{\nu}{a}\right).\end{aligned} \tag{24}$$

Thus, $\int_{-\infty}^{\infty}\int_{-\infty}^{\infty}B'_\theta(\omega,\nu)d\omega d\nu = a^{-4}\int_{-\infty}^{\infty}\int_{-\infty}^{\infty}B_\theta(\omega,\nu)d\omega d\nu$. When computing $\Phi'(\theta)$, the constant multiplier a^{-4} will be cancelled out, which means that $\Phi(\theta)$ is scaling invariant.

According to the periodicity and symmetry of the Radon transform, we have

$$R(s,\theta) = \begin{cases} R(s,\theta+2n\pi),\\ R(-s,\theta+(2n+1)\pi),\end{cases} \tag{25}$$

where n is an integer. Thus, $\Phi(\theta)=\Phi(\theta+2n\pi)$. $R(-s,\theta+(2n+1)\pi)$ can be seen as a special case of Eq. (17), where $a=-1$ and the Radon transform is done at the angle $\theta+(2n+1)\pi$. Then, using Theorem 2, $\Phi(\theta)=\Phi(\theta+(2n+1)\pi)$. Therefore, we have

Corollary 1. $\Phi(\theta)$ is periodic with period π, i.e., $\Phi(\theta)=\Phi(\theta+n\pi)$.

If the original image is rotated by an angle θ_0, using Eq. (18), the Radon transform $R'(s,\theta)$ of the rotated image can be written as $R'(s,\theta)=R(s,\theta+\theta_0)$, which implies that the rotation of the image leads to a cyclically shifted $\Phi(\theta)$ by an amount θ_0 in the cycle period $[0,\pi)$. Several techniques can be used to eliminate the effect of cyclic shift. In this paper, a reference angle of $\Phi(\theta)$, denoted by $\overline{\theta}$, is defined as

$$\overline{\theta} = \frac{1}{2}angle\left(\frac{\int_0^\pi e^{i2\theta}||\Phi(\theta)||_1 d\theta}{\int_0^\pi ||\Phi(\theta)||_1 d\theta}\right), \tag{26}$$

where $angle(\cdot)$ is the phase angle of a complex number, and $||\cdot||_1$ is the sum of the absolute value of each component for a quaternion. If $\Phi(\theta')$ is a cyclically shifted version of $\Phi(\theta)$, where $\theta'=\theta+\theta_0$, by Eq. (26), the reference angle $\overline{\theta'}$ of $\Phi(\theta')$ is

$$\begin{aligned}\overline{\theta'} &= \frac{1}{2}\,\text{angle}\left(\frac{\int_0^\pi e^{i2\theta}||\Phi(\theta+\theta_0)||_1 d\theta}{\int_0^\pi ||\Phi(\theta+\theta_0)||_1 d\theta}\right)\\ &= \frac{1}{2}\,\text{angle}\left(e^{-i2\theta_0}\frac{\int_0^\pi e^{i2\theta}||\Phi(\theta)||_1 d\theta}{\int_0^\pi ||\Phi(\theta)||_1 d\theta}\right)\\ &= \overline{\theta}-\theta_0.\end{aligned} \tag{27}$$

Thus, $\Phi(\overline{\theta'}+\theta_0)=\Phi(\overline{\theta})$. Then, we can obtain the rotation invariants by cyclically shifting the sequence $\Phi(\theta)$ in $[0,\pi)$ to the reference angle $\overline{\theta}$.

3.3. Feature reduction using quaternion principal component analysis (QPCA)

In general, the number of features may be large at the feature generation stage. The main task of feature reduction is to reduce the redundant information contained in each pair of different features by removing the correlation between them and select features with large interclass separation, both of which can be achieved through QPCA [29].

Suppose that we have M number of image classes and N_m number of sample images for the mth image class. The $L-D$ feature vector generated using the QHOS invariants algorithm for each sample is denoted by $\Phi_n^m(n=1,\ldots,N_m,\ m=1,\ldots,M)$. The feature covariance matrix$C$in the feature space is defined by

$$C = \frac{1}{M}\sum_{m=1}^{M}(\overline{\Phi}^m-\overline{\Phi})(\overline{\Phi}^m-\overline{\Phi})^H, \tag{28}$$

where H denotes the conjugate transpose operation, and $\overline{\Phi}^m$, $\overline{\Phi}$ are given by

$$\overline{\Phi}^m = \frac{1}{N_m}\sum_{n=1}^{N_m}\Phi_n^m, \tag{29}$$

$$\overline{\Phi} = \frac{1}{M}\sum_{m=1}^{M}\overline{\Phi}^m. \tag{30}$$

Since C is an $L\times L$ self-conjugate symmetric matrix, it possesses L real eigenvalues. Then, feature reduction can be achieved by projecting each feature vector Φ_n^m from the $L-D$ space onto an $l-D(l<L)$ space using the Hotelling transform as follows:

$$V_n^m = U^H(\Phi_n^m-\overline{\Phi}), \tag{31}$$

where U is an $L\times l$ matrix consisting of the eigenvectors corresponding to the first l largest eigenvalues of C in descending order.

4. Experiments

This section is intended to test the invariance property of the proposed quaternion higher-order spectra invariants (QHOSIs) to various geometric transformations and their robustness to different types of noises. In the following subsections, the unit pure quaternions $\mu=(i+j+k)/\sqrt{3}$ and $\mu_1=(i+j-2k)/\sqrt{6}$ are chosen to compute QHOSIs, and the central slice is computed at the angle varying from 6° to 180° every 6°. The Quaternion Toolbox for Matlab [30] is used in implementing the quaternion arithmetic.

4.1. Test of invariance to RTS transformations

We first validate the performance of the proposed QHOSIs with respect to RTS transformations. The standard color Lena and Peppers images of size 128×128 were undergone different geometric transformations. In order to contain the entire transformed standard color images, the actual size of the original images (without any geometric transformations) is changed into 208×208 by adding some background pixels around the standard color images. Then each image was translated with $\Delta x\in\{-29,-27,\ldots,29\}$, $\Delta y\in\{-29,-27,\ldots,29\}$, rotated with $\alpha\in\{0°,12°,\ldots,348°\}$, and scaled with scaling factor $\lambda\in\{0.1,0.2,\ldots,3\}$, forming four sets of 30 images for Lena and Peppers, respectively. Fig. 1 shows some examples of the transformed images.

The proposed QHOSIs defined in Eq. (22) are calculated for each transformed image. Figs. 2 and 3 show the second and fourth components of the calculated QHOSIs at the reference angle $\overline{\theta}$ for the Lena and Peppers images, respectively, from which we can see that excellent results have been obtained. Table 1 shows the absolute values of σ/ε to indicate the stability of the invariants in Figs. 2 and 3, where σ and ε denote the standard deviation and mean of the invariants, respectively. It can be seen from Table 1 that most of the values of $|\sigma/\varepsilon|$ are less than 2%. Therefore, the QHOS invariants derived in this paper could be a useful tool in color image recognition tasks that require invariance to RTS transformations.

4.2. Test of robustness against background noise

In this subsection, our purpose is to test the robustness of the proposed QHOSIs against some frequently encountered additive noise, including white Gaussian, uniform and exponential noise. The original images are the standard color Barbara and Boats

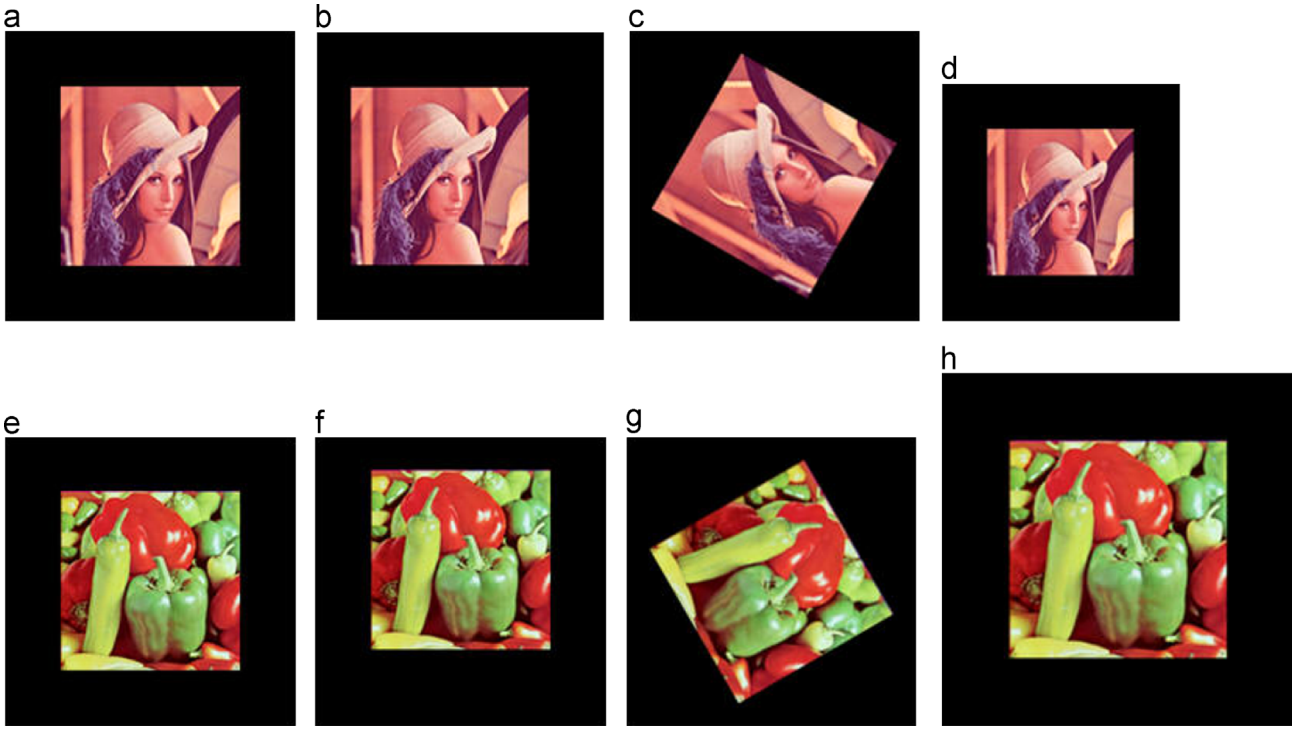

Fig. 1. Examples of the standard color Lena and Peppers images with different geometric transformations. (a) Original image. (b) $\Delta x=-15$, (c) $\alpha=60^{\circ}$, (d) $\lambda=0.8$, (e) original image, (f) $\Delta y=-15$, (g) $\alpha=300^{\circ}$ and (h) λ=1.2. (For interpretation of the references to color in this figure legend, the reader is referred to the web version of this article.)

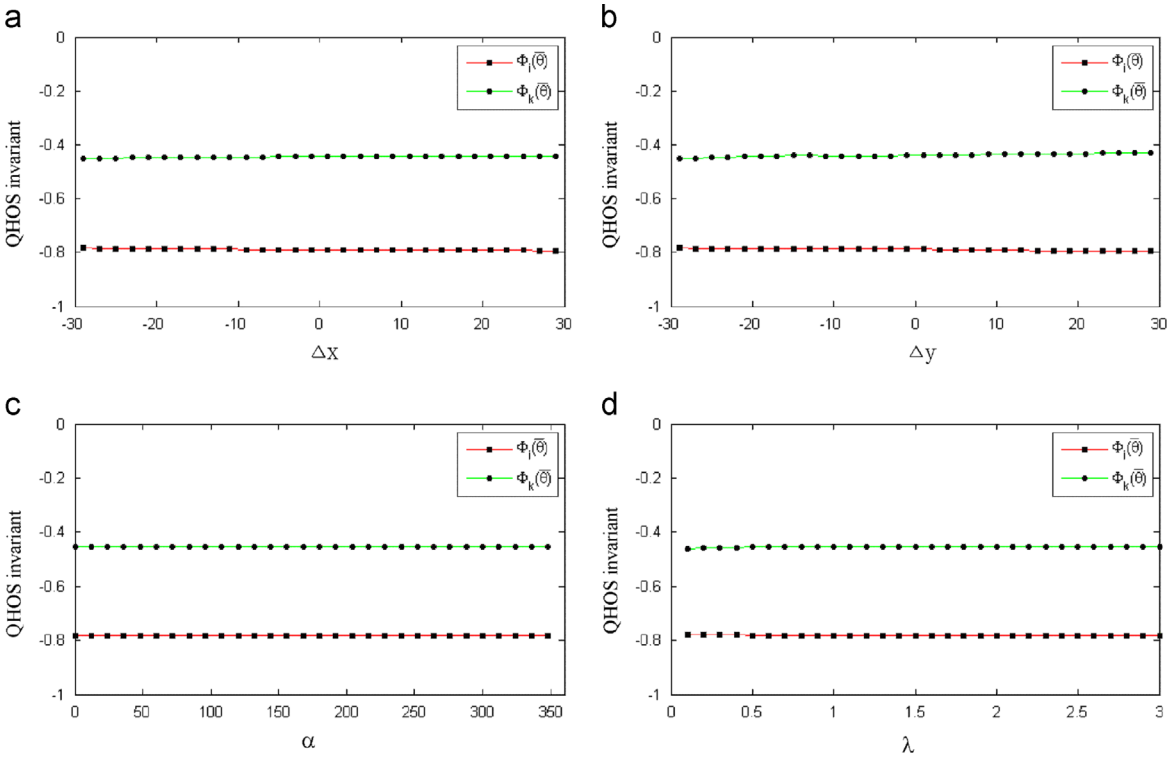

Fig. 2. The second and fourth components of the QHOS invariants at the reference angle $\bar{\theta}$ for the standard color Lena image under different geometric transformations: (a) translated along the x-axis with $\Delta x\in\{-29,-27,\ldots,29\}$; (b) translated along the y-axis with $\Delta y\in\{-29,-27,\ldots,29\}$; (c) rotated with $\alpha\in\{0^{\circ},12^{\circ},\ldots,348^{\circ}\}$; (d) scaled with $\lambda\in\{0.1,0.2,\ldots,3\}$. (For interpretation of the references to color in this figure legend, the reader is referred to the web version of this article.)

images of size 128×128. Each type of noise mentioned above with different standard deviations (STDs) was added to the original images. Examples of the corrupted images and experimental results are shown in Fig. 4 and Tables 2 and 3, respectively.

To quantify the robustness of our proposed QHOSIs, a comparative test is also conducted involving the quaternion Fourier–Mellin moment invariants (QFMMIs) method [21]. The experiment described above is repeated using QFMMIs and the corresponding results are depicted in Tables 4 and 5. It can be concluded from Tables 2–5 that the QHOSIs remain almost unchanged ($|\sigma/\varepsilon|\leq2\%$) and perform better than the QFMMIs ($|\sigma/\varepsilon|\leq16\%$) in the presence of each type of noise.

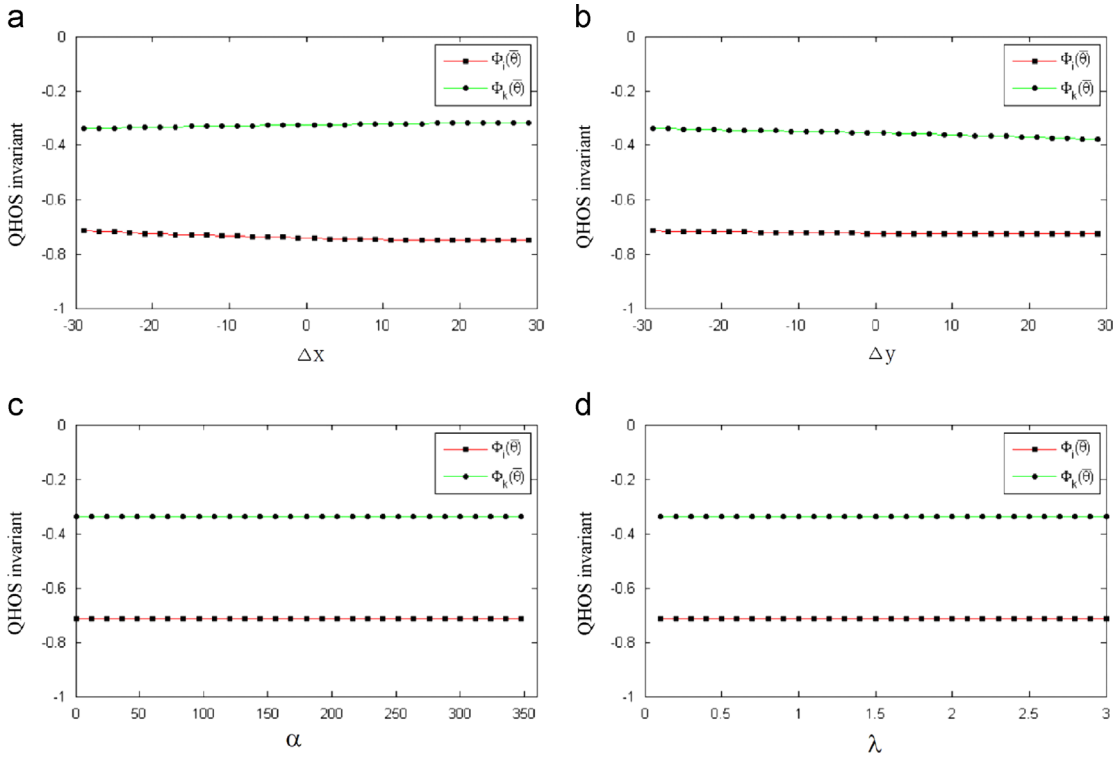

Fig. 3. The second and fourth components of the QHOS invariants at the reference angle $\bar{\theta}$ for the standard color Peppers image under different geometric transformations: (a) translated along the x-axis with $\Delta x \in \{-29, -27, \ldots, 29\}$; (b) translated along the y-axis with $\Delta y \in \{-29, -27, \ldots, 29\}$; (c) rotated with $\alpha \in \{0^\circ, 12^\circ, \ldots, 348^\circ\}$; (d) scaled with $\lambda \in \{0.1, 0.2, \ldots, 3\}$. (For interpretation of the references to color in this figure legend, the reader is referred to the web version of this article.)

Table 1
The absolute values of σ/ε (%) to indicate the stability of the QHOSIs in Figs. 2 and 3.

$\lvert\sigma/\varepsilon\rvert$ (%)	Fig. 2(a)	Fig. 2(b)	Fig. 2(c)	Fig. 2(d)	Fig. 3(a)	Fig. 3(b)	Fig. 3(c)	Fig. 3(d)
$\Phi_i(\bar{\theta})$	0.3066	0.4540	0.0018	0.1183	1.5546	0.4945	0.0025	0.0162
$\Phi_k(\bar{\theta})$	0.6043	1.2776	0.0079	0.4897	2.0217	3.2981	0.0055	0.0282

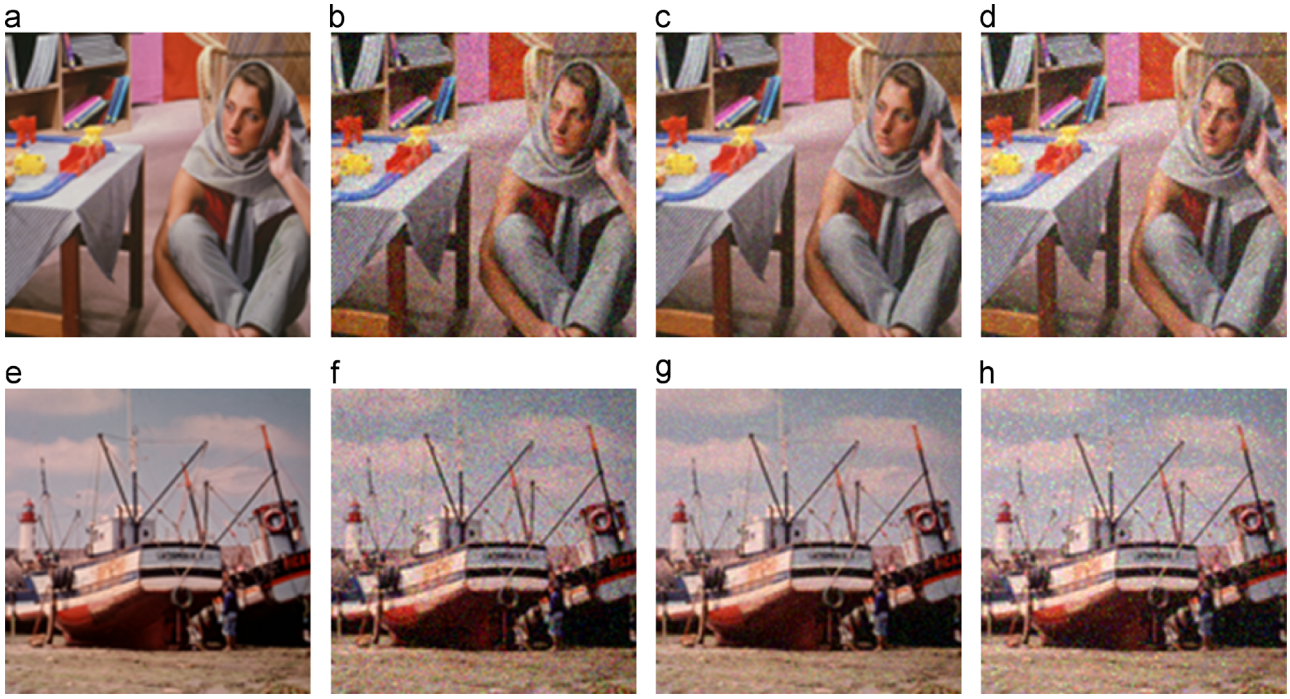

Fig. 4. Examples of the standard color Barbara and Boats images corrupted by additive Gaussian, uniform and exponential noise with STD=15. (a) Original image, (b) gaussian noise (STD=15), (c) uniform noise (STD=15), (d) exponential noise (STD=15), (e) original image, (f) gaussion noise (STD=15), (g) uniform noise (STD=15) and (h) exponential nosie (STD=15). (For interpretation of the references to color in this figure legend, the reader is referred to the web version of this article.)

Table 2
The second and third components of the QHOS invariants at the reference angle $\bar{\theta}$ for the standard color Barbara image corrupted by additive Gaussian, uniform and exponential noise with different STDs.

	Gaussian noise		Uniform noise		Exponential noise	
	$\Phi_i(\bar{\theta})$	$\Phi_j(\bar{\theta})$	$\Phi_i(\bar{\theta})$	$\Phi_j(\bar{\theta})$	$\Phi_i(\bar{\theta})$	$\Phi_j(\bar{\theta})$
STD=35	−0.6831	−0.5325	−0.6724	−0.5395	−0.6588	−0.5463
STD=30	−0.6839	−0.5325	−0.6752	−0.5380	−0.6617	−0.5448
STD=25	−0.6829	−0.5337	−0.6761	−0.5372	−0.6654	−0.5431
STD=20	−0.6846	−0.5331	−0.6774	−0.5374	−0.6699	−0.5409
STD=15	−0.6845	−0.5339	−0.6792	−0.5363	−0.6732	−0.5400
STD=10	−0.6850	−0.5338	−0.6813	−0.5351	−0.6770	−0.5372
STD=5	−0.6847	−0.5333	−0.6829	−0.5344	−0.6807	−0.5358
STD=0	−0.6847	−0.5335	−0.6847	−0.5335	−0.6847	−0.5335
σ/ε (%)	−0.1173	−0.1034	−0.6118	−0.3687	−1.3630	−0.8252

Table 3
The second and third components of the QHOS invariants at the reference angle $\bar{\theta}$ for the standard color Boats image corrupted by additive Gaussian, uniform and exponential noise with different STDs.

	Gaussian noise		Uniform noise		Exponential noise	
	$\Phi_i(\bar{\theta})$	$\Phi_j(\bar{\theta})$	$\Phi_i(\bar{\theta})$	$\Phi_j(\bar{\theta})$	$\Phi_i(\bar{\theta})$	$\Phi_j(\bar{\theta})$
STD=35	−0.6359	−0.5476	−0.6304	−0.5508	−0.6242	−0.5550
STD=30	−0.6354	−0.5478	−0.6323	−0.5500	−0.6258	−0.5536
STD=25	−0.6351	−0.5476	−0.6326	−0.5503	−0.6277	−0.5526
STD=20	−0.6357	−0.5476	−0.6327	−0.5505	−0.6292	−0.5526
STD=15	−0.6362	−0.5476	−0.6339	−0.5494	−0.6297	−0.5520
STD=10	−0.6358	−0.5481	−0.6343	−0.5492	−0.6328	−0.5501
STD=5	−0.6360	−0.5481	−0.6351	−0.5488	−0.6344	−0.5489
STD=0	−0.6357	−0.5483	−0.6357	−0.5483	−0.6357	−0.5483
σ/ε (%)	−0.0532	−0.0524	−0.2729	−0.1632	−0.6519	−0.4215

Table 4
QFMM invariants for the standard color Barbara image corrupted by additive Gaussian, uniform and exponential noise with different STDs.

	Gaussian noise		Uniform noise		Exponential noise	
	$\Phi_{1,1}$	$\Phi_{1,2}$	$\Phi_{1,1}$	$\Phi_{1,2}$	$\Phi_{1,1}$	$\Phi_{1,2}$
STD=35	0.0089	0.0309	0.0059	0.0267	0.0063	0.0245
STD=30	0.0082	0.0320	0.0070	0.0283	0.0068	0.0244
STD=25	0.0069	0.0319	0.0071	0.0278	0.0059	0.0262
STD=20	0.0068	0.0297	0.0069	0.0281	0.0070	0.0264
STD=15	0.0057	0.0305	0.0062	0.0289	0.0061	0.0261
STD=10	0.0061	0.0304	0.0061	0.0296	0.0067	0.0287
STD=5	0.0065	0.0301	0.0064	0.0300	0.0067	0.0294
STD=0	0.0063	0.0306	0.0063	0.0306	0.0063	0.0306
σ/ε (%)	15.5837	2.6742	6.9603	4.4710	6.0911	8.4694

Table 5
QFMM invariants for the standard color Boats image corrupted by additive Gaussian, uniform and exponential noise with different STDs.

	Gaussian noise		Uniform noise		Exponential noise	
	$\Phi_{1,1}$	$\Phi_{1,2}$	$\Phi_{1,1}$	$\Phi_{1,2}$	$\Phi_{1,1}$	$\Phi_{1,2}$
STD=35	0.0530	0.0381	0.0500	0.0381	0.0398	0.0317
STD=30	0.0548	0.0396	0.0495	0.0396	0.0421	0.0316
STD=25	0.0529	0.0396	0.0520	0.0395	0.0439	0.0334
STD=20	0.0550	0.0414	0.0521	0.0411	0.0480	0.0357
STD=15	0.0567	0.0429	0.0547	0.0416	0.0501	0.0372
STD=10	0.0574	0.0441	0.0559	0.0429	0.0534	0.0405
STD=5	0.0581	0.0445	0.0569	0.0438	0.0553	0.0426
STD=0	0.0585	0.0451	0.0585	0.0451	0.0585	0.0451
σ/ε (%)	3.9567	6.2152	6.1760	5.7007	13.6501	13.6581

4.3. Color object recognition

To further evaluate the performance of the proposed QHOSIs to RTS transformations and their robustness against noise, color object recognition procedure was conducted. Twelve images with size 128×128 selected from the public Columbia Object Image Library (COIL) database [31] were used as the training set, meaning that one sample image per image class. The actual size of all the original images is 208×208 by adding a black background (Fig. 5) and a real-word background (Fig. 6), respectively. Then each image was translated with $\Delta x = 8$, $\Delta y = 6$, rotated with angle $\alpha \in \{0, 30, \ldots, 150\}$, and scaled with scale factor $\lambda \in \{0.5, 0.75, \ldots, 2.0\}$, forming 42 realizations per image class. A testing set of 504 images was obtained by adding a white Gaussian noise, a uniform noise or an exponential noise with different STDs to those realizations mentioned above. First, a 30-D feature vector for each transformed and corrupted image was generated using the QHOSIs generation method. Then, the feature reduction algorithm was applied with different values of l (the number of features derived using QPCA). At last, the minimum Euclidean distance was used as the classifier.

The resultant recognition rates for the images in Fig. 5 with different values of l under additive white Gaussian noise are listed in Table 6, which shows that the best performance is obtained when $l = 3$. Fig. 7 illustrates an example of scatter plots of the first QHOSI derived at $l = 3$ for the images in Fig. 5 corrupted by Gaussian noise with different STDs. As can be observed, the derived features are consistent with human's visual perception in the sense that the distance between the feature vectors of two visually similar images is smaller than the distance between those of the dissimilar images.

In order to compare the recognition efficiency of our QHOSIs, the experiments described above are also repeated using the quaternion Zernike moment invariants (QZMIs) method proposed in [22]. The resultant recognition rates using QHOSIs and QZMIs under additive white Gaussian, uniform and exponential noise with different STDs are summarized in Tables 7 and 8 for images in Figs. 5 and 6, respectively. It can be concluded from these results that: (1) the performance of QHOSIs in the presence of uniform noise is comparable with that obtained for white Gaussian noise; (2) the QHOSIs do not have the same success for exponential noise, because the distribution of such noise is not symmetrical; (3) the recognition rates for objects in Fig. 5 are generally higher than those in Fig. 6, because RTS transformations lead to more changes in real-word backgrounds; and (4) the performance of QHOSIs is better than the QZMIs in the presence of each type of noise, especially in the presence of noises with high STDs.

4.4. Noisy color texture recognition

Noisy texture recognition is more difficult due to the fact that detailed texture structure is more vulnerable to background noise. However, most denoizing methods for texture images make the

Fig. 5. Twelve color objects with a black background selected from the Columbia University Image Library database. (For interpretation of the references to color in this figure legend, the reader is referred to the web version of this article.)

Fig. 6. Twelve color objects with a real-word background. (For interpretation of the references to color in this figure legend, the reader is referred to the web version of this article.)

Table 6
Recognition rates (%) using QHOS invariants under additive Gaussian noise with different STDs. l is the number of derived quaternion-valued features.

	$l=1$	$l=2$	$l=3$	$l=4$	$l=6$	$l=30$
STD=1	100.00	100.00	100.00	100.00	100.00	100.00
STD=3	100.00	100.00	100.00	100.00	100.00	100.00
STD=5	100.00	99.80	99.80	100.00	99.60	99.21
STD=7	98.81	99.60	99.60	99.60	99.21	97.42
STD=10	95.63	97.82	97.82	95.63	94.44	87.90
STD=15	91.67	93.45	93.45	87.90	85.32	80.56
STD=20	78.57	84.13	83.93	83.53	79.56	78.57
STD=25	76.39	83.13	83.53	83.53	78.57	77.58
Average rate	92.63	94.74	94.77	93.77	92.09	90.15

resultant images lose the textural structure. In our study, it has been shown that QHOSIs are robust to different types of noises. In addition, due to the use of the Radon transform, QHOSIs contain inner structural details about a given image. Thus, we expect that the proposed invariants generation method can be extended to noisy color texture recognition. By proceeding in a similar way as that described in Section 3 for color images, we can also derive the HOSIs for each channel of an RGB image (denoted hereafter by DHOSIs) and the gray-scale image obtained by image graying (denoted hereafter by GHOSIs). In order to compare the proposed QHOSIs with DHOSIs and GHOSIs in terms of recognition accuracy, we use the values of l (the number of features derived using PCA) with the best performances in all experiments.

Sixteen color texture images with size 128×128 (Fig. 8) selected from the VisTex database [32] were used. Each image was transformed with the same transformations as those presented in Section 4.3. This was followed by adding a white Gaussian noise, a uniform noise or an exponential noise with different STDs. The recognition results are shown in Table 9. We can conclude that the QHOSIs yield good performance for noisy

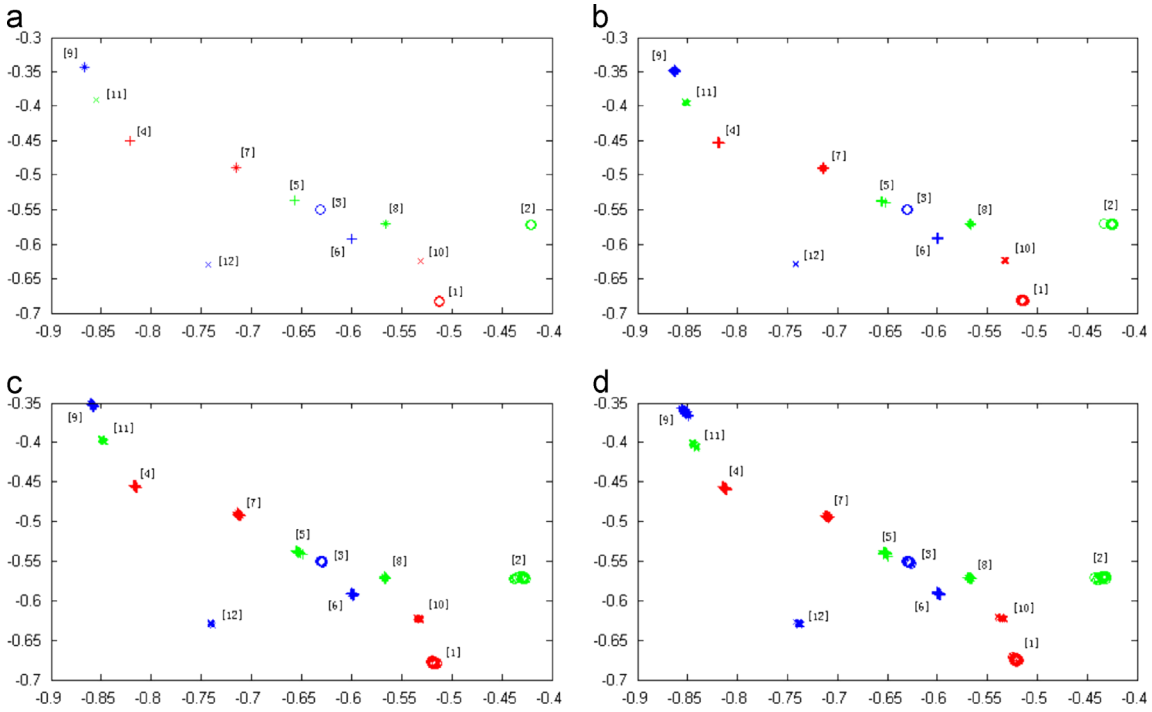

Fig. 7. Cluster plots of the second (horizontal axis) and third (vertical axis) components of the first QHOS invariant for the twelve color objects in Fig. 5 corrupted by Gaussian noise with different STDs: (a) STD=0; (b) STD=5; (c) STD=10; (d) STD=15.

Table 7
Recognition rates (%) using QHOS invariants and QZM invariants for color objects with a black background under additive Gaussian, uniform and exponential noise with different STDs.

	Gaussian noise		Uniform noise		Exponential noise	
	QHOSIs	QZMIs	QHOSIs	QZMIs	QHOSIs	QZMIs
STD=1	100.00	100.00	100.00	100.00	100.00	100.00
STD=3	100.00	95.67	100.00	95.04	92.86	88.04
STD=5	99.80	86.72	99.80	85.91	84.33	78.91
STD=7	99.60	82.59	99.40	83.33	82.33	76.33
STD=10	97.82	80.99	97.62	80.16	75.00	73.16
STD=15	93.45	62.96	96.23	62.70	66.67	55.70
STD=20	83.93	46.62	95.04	47.42	58.13	40.42
STD=25	83.53	38.25	93.25	38.69	49.40	31.69
Average rate	94.77	74.22	97.67	74.16	76.09	68.03

Table 8
Recognition rates (%) using QHOS invariants and QZM invariants for color objects with a real-word background under additive Gaussian, uniform and exponential noise with different STDs.

	Gaussian noise		Uniform noise		Exponential noise	
	QHOSIs	QZMIs	QHOSIs	QZMIs	QHOSIs	QZMIs
STD=1	100.00	100.00	100.00	100.00	100.00	100.00
STD=3	100.00	90.13	100.00	91.64	85.32	84.06
STD=5	99.21	81.83	99.60	81.20	80.16	74.13
STD=7	97.42	79.26	98.21	79.18	77.98	71.40
STD=10	87.90	74.47	96.43	76.99	69.44	67.12
STD=15	80.95	58.64	92.06	59.28	65.08	51.12
STD=20	79.17	43.33	91.07	44.34	60.52	35.85
STD=25	78.17	33.66	87.50	35.00	49.01	26.88
Average rate	90.35	70.17	95.61	70.95	73.44	63.82

color texture recognition without employing noise reduction procedure and perform much better than the other two methods, especially than GHOSIs. The reason is that graying loses some color information, which may be important in color texture recognition.

5. Conclusions

In this paper, we have extended the conventional higher-order spectra from real numbers to quaternion algebra. Quaternion

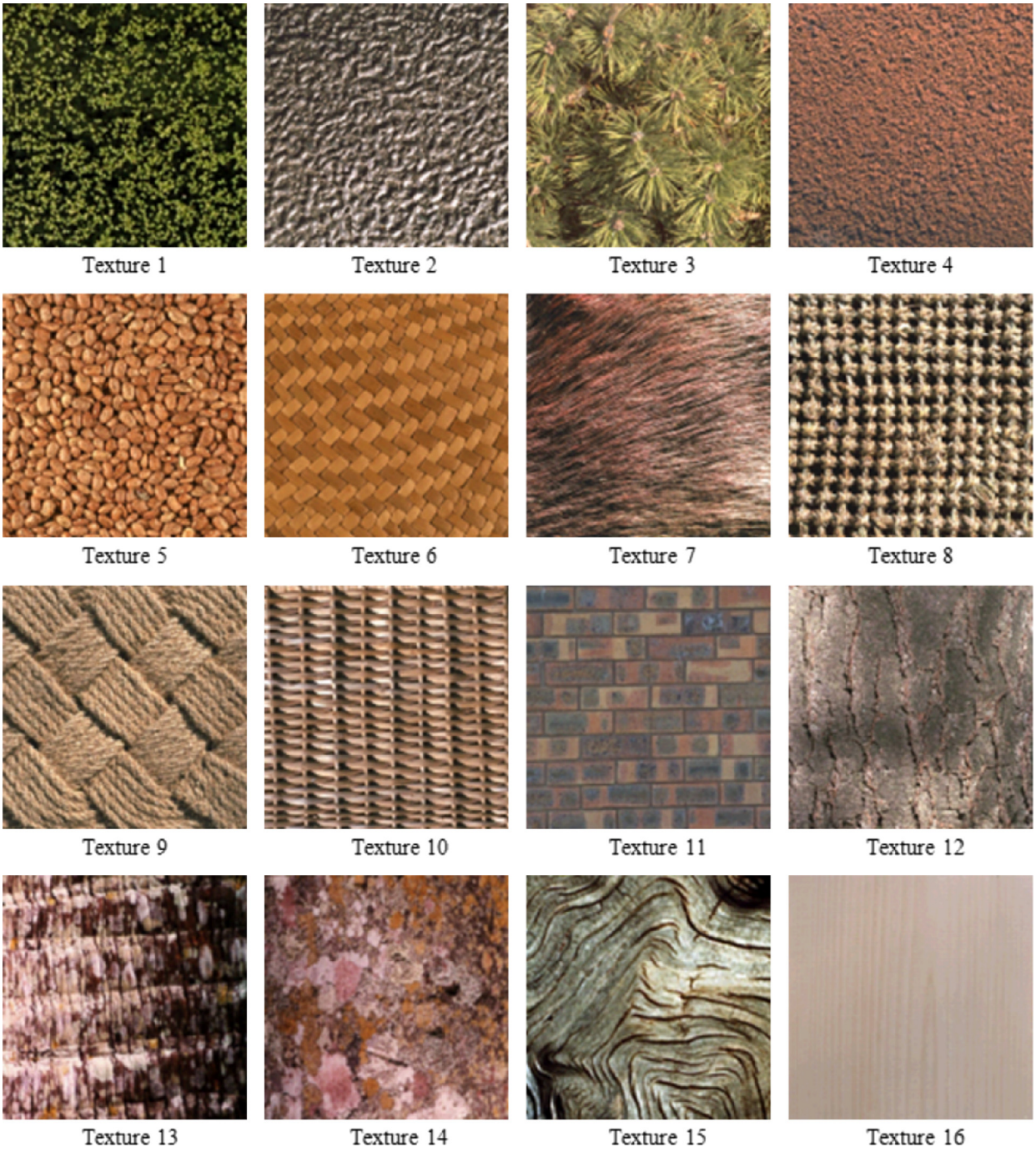

Fig. 8. Sixteen color texture images selected from the VisTex database. (For interpretation of the references to color in this figure legend, the reader is referred to the web version of this article.)

Table 9
Recognition rates (%) using QHOS invariants, DHOS invariants and GHOS invariants under additive Gaussian, uniform and exponential noise with different STDs.

	Gaussian noise			Uniform noise			Exponential noise		
	QHOSIs	DHOSIs	GHOSIs	QHOSIs	DHOSIs	GHOSIs	QHOSIs	DHOSIs	GHOSIs
STD=1	100.00	99.01	80.80	100.00	99.40	80.36	100.00	98.60	72.17
STD=3	100.00	96.61	69.05	99.70	95.68	68.15	84.32	81.55	48.07
STD=5	96.88	92.49	52.08	98.07	93.01	55.95	78.16	71.28	33.93
STD=7	95.20	86.93	48.96	97.02	86.90	51.79	72.98	68.75	30.21
STD=10	85.08	83.64	40.03	94.35	82.14	41.82	65.44	54.14	23.36
STD=15	78.39	71.88	32.14	90.33	72.77	31.85	53.08	47.35	22.77
STD=20	77.29	58.01	27.53	87.50	67.26	26.93	49.52	39.80	21.43
STD=25	72.17	55.48	24.70	84.38	60.27	25.74	41.01	31.25	17.56
Average rate	88.13	80.50	46.91	93.92	82.18	47.82	68.06	61.59	33.69

higher-order spectra invariants (QHOSIs) with respect to RTS transformations have been constructed. The generated QHOSIs are further reduced to a smaller set by means of quaternion principal component analysis. The proposed PR system based on QHOSIs has been tested against color objects and textures. It has been shown that QHOSIs are more robust to background noise, especially to symmetrically distributed ones. Further, by means of quaternion principal component analysis, the reduced feature set contains no redundant information in the sense that feature elements are uncorrelated with each other. Therefore, the proposed method has more discriminative power than the existing methods. The feature vector is computed only once for each image class in the training process and stored along with the model image for later classification, which keeps the computational complexity of the integrated algorithm reasonable for many practical applications. Our future work will focus on studying the potential symmetry of QHOS to further reduce the amount of calculation and constructing QHOS invariants with respect to other geometric transformations such as shearing and perspective.

Acknowledgement

The authors would like to thank the anonymous reviewers and editors for their work. This work was supported by 985 Project of Jilin University.

Appendix A

QUATERNIONS A quaternion q is a 4-D number, having one real part and three imaginary parts, which can be written as

$$q = q_r + q_i i + q_j j + q_k k, \tag{A1}$$

where q_r, q_i, q_j, q_k are real, and i, j, k are complex operators obeying the following rules:

$$i^2 = j^2 = k^2 = -1, ij = -ji = k, jk = -kj = i, ki = -ik = j. \tag{A2}$$

It can be seen from Eq. (A2) that the multiplication of quaternions is not commutative. When $q_r = 0$, q is referred to as a pure quaternion.

The conjugate and norm of a quaternion are respectively defined as follows:

$$\overline{q} = q_r - q_i i - q_j j - q_k k, \tag{A3}$$

$$||q|| = \sqrt{q\overline{q}} = \sqrt{q_r^2 + q_i^2 + q_j^2 + q_k^2}. \tag{A4}$$

when $||q|| = 1$, q is called as a unit quaternion.

Euler′s formula holds for quaternions, that is

$$e^{\mu\varphi} = \cos\varphi + \mu \sin\varphi, \tag{A5}$$

where μ is a unit pure quaternion.

Let $f(x,y)$ be a 2-D quaternion-valued function, due to the noncommutative property of quaternion multiplication, there are three different definitions of 2-D quaternion Fourier transforms (QFTs) as follows:

$$F^R(\omega,\nu) = \int_{-\infty}^{\infty}\int_{-\infty}^{\infty} f(x,y) e^{-\mu_1(\omega x + \nu y)} dxdy, \tag{A6}$$

$$F^L(\omega,\nu) = \int_{-\infty}^{\infty}\int_{-\infty}^{\infty} e^{-\mu_2(\omega x + \nu y)} f(x,y) dxdy, \tag{A7}$$

$$F^{RL}(\omega,\nu) = \int_{-\infty}^{\infty}\int_{-\infty}^{\infty} e^{-\mu_2\omega x} f(x,y) e^{-\mu_1\nu y} dxdy, \tag{A8}$$

where μ_1 and μ_2 are two unit pure quaternions that are orthogonal to each other, and $F^R(\omega,\nu)$, $F^L(\omega,\nu)$ and $F^{RL}(\omega,\nu)$ are called right-side, left-side and two-side QFTs, respectively.

References

[1] Wood J. Invariant pattern recognition: a review. Pattern Recognit 1996;29:1–17.
[2] Granlund GH. Fourier preprocessing for hand print character recognition. IEEE Trans Comput 1972;21:195–201.
[3] Zahn CT, Roskies RZ. Fourier descriptors for plane closed curves. IEEE Trans Comput 1972;21:269–81.
[4] Crimmins TR. A complete set of Fourier descriptors for two-dimensional shapes. IEEE Trans Syst Man Cybern 1982;12:848–55.
[5] Persoon E, Fu KS. Shape discrimination using Fourier descriptors. IEEE Trans Syst Man Cybern 1977;7:388–97.
[6] Hu MK. Visual pattern recognition by moment invariants. IRE Trans Inf Theory 1962;8:179–87.
[7] Liu J, Zhang TX. Fast algorithm for generation of moment invariants. Pattern Recognit 2004;37:1745–56.
[8] Flusser J, Suk T. Pattern recognition by affine moment invariants. Pattern Recognit 1993;26:167–74.
[9] Flusser J. On the independence of rotation moment invariants. Pattern Recognit 2000;33:1405–10.
[10] Kim YC, Powers EJ. Digital bispectral analysis and its applications to nonlinear wave interactions. IEEE Trans Plasma Sci 1979;7:120–31.
[11] Giannakis GB. Cumulants: a powerful tool in signal processing. Proc IEEE 1987;75:1333–4.
[12] Chandran V, Elgar S. Bispectral analysis of two-dimensional random processes. IEEE Trans Acoust Speech Signal Process 1990;38:2181–6.
[13] Tsatsanis MK, Giannakis GB. Translation, rotation and scaling invariant object and texture classification using polyspectra. Proc SPIE Int Soc Opt Eng 1990;1348:103–15.
[14] Chandran V, Elgar SL. Pattern recognition using invariants defined from higher order spectra—1-D inputs. IEEE Trans Signal Process 1993;41:205–11.
[15] Chandran V, Boashash B, Elgar S. Pattern recognition using invariants defined from higher order spectra—2-D image inputs. IEEE Trans Image Process 1997;6:703–11.
[16] Shao Y, Celenk M. Higher-order spectra (HOS) invariants for shape recognition. Pattern Recognit 2001;34(11):2097–113.
[17] Kantor IL, Solodovnikov AS. Hypercomplex number: an elementary introduction to algebras. New York: Springer-Verlag; 1989.
[18] Ell, TA. Hypercomplex spectral transforms. PhD dissertation. Minneapolis, Minnesota University; 1992.
[19] Sangwine SJ. Fourier transforms of colour images using quaternion or hypercomplex numbers. Electron Lett 1996;32:1979–80.
[20] Ell TA, Sangwine SJ. Hypercomplex Fourier transforms of color images. IEEE Trans Image Process 2007;16:22–35.
[21] Guo LQ, Zhu M. Quaternion Fourier–Mellin moments for color images. Pattern Recognit 2011;44:187–95.
[22] Chen BJ, Shu HZ, Zhang H, Chen G, Toumoulin C, Dillenseger JL, et al. Quaternion Zernike moments and their invariants for color image analysis and object recognition. Sign Proces 2012;92:308–18.
[23] Wang Q, Wang ZZ. Color image registration based on quaternion Fourier transformation. Opt Eng 2012;51(5):057002.
[24] Ma XJ, Xu Y, Song L, Yang XK, Burkhardt H. Color image watermarking using local quaternion Fourier spectral analysis, Proceedings of the IEEE international conference on multimedia and expo (ICME2008), 2008, 233–236.
[25] Alexiadis DS, Sergiadis GD. Estimation of motions in color image sequences using hypercomplex Fourier transforms. IEEE Trans Image Process 2009;18 (1):168–87.
[26] Assefa D, Mansinha L, Tiampo KF, Rasmussen H, Abdella K. Local quaternion Fourier transform and color image texture analysis. Signal Process 2010;90:1825–35.
[27] Ward JP. Quaternions and Cayley numbers, algebra and applications. Norwell, MA: Kluwer; 1997.
[28] Nikias CL, Petropulu AP. Higher order spectra analysis. Englewood Cliffs: Prentice Hall; 1993.
[29] Le Bihan N, Sangwine SJ. Quaternion principal component analysis of color images. IEEE International Conference on Image Proce, (ICIP) 2003;1:809–12.
[30] Sangwine S, LeBihan N. Quaternion toolbox for Matlab, ⟨http://qtfm.sourceforge.net/⟩.
[31] Nene SA, Nayar SK, Murase H. Columbia object image library (COIL-100), technical report CUCS-006-96, 1996, ⟨http://www.cs.columbia.edu/CAVE/software/softlib/coil-100.php⟩.
[32] VisTex Vision Texture database, vision and modeling group, MIT Media Laboratory, 1995, ⟨http://vismod.media.mit.edu/pub/VisTex/⟩.